Stabilizing a Double Gyroid Network Phase with 2 nm Feature Size by Blending of Lamellar and Cylindrical Forming Block Oligomers

Zhengyuan Shen, Ke Luo, So Jung Park, Daoyuan Li, Mahesh K. Mahanthappa, Frank S. Bates, Kevin D. Dorfman, Timothy P. Lodge,* and J. Ilja Siepmann*

Read Online

ACCESS | ◫ Metrics & More | ◨ Article Recommendations | SI Supporting Information

ABSTRACT: Molecular dynamics simulations are used to study binary blends of an AB-type diblock and an AB_2-type miktoarm triblock amphiphiles (also known as high-χ block oligomers) consisting of sugar-based (A) and hydrocarbon (B) blocks. In their pure form, the AB diblock and AB_2 triblock amphiphiles self-assemble into ordered lamellar (LAM) and cylindrical (CYL) structures, respectively. At intermediate compositions, however, the AB_2-rich blend ($0.2 \leq x_{AB} \leq 0.4$) forms a double gyroid (DG) network, whereas perforated lamellae (PL) are observed in the AB-rich blend ($0.5 \leq x_{AB} \leq 0.8$). All of the ordered mesophases present domain pitches under 3 nm, with 1 nm feature sizes for the polar domains. Structural analyses reveal that the nonuniform interfacial curvatures of DG and PL structures are supported by local composition variations of the LAM- and CYL-forming amphiphiles. Self-consistent mean field theory calculations for blends of related AB and AB_2 block polymers also show the DG network at intermediate compositions, when A is the minority block, but PL is not stable. This work provides molecular-level insights into how blending of shape-filling molecular architectures enables network phase formation with extremely small feature sizes over a wide composition range.
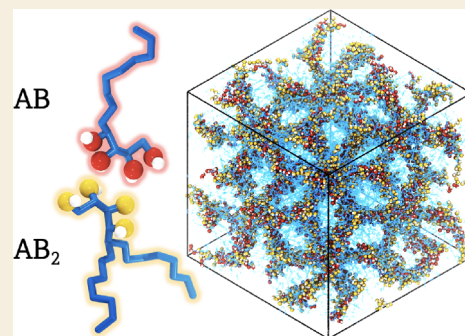
KEYWORDS: Continuous Network Phases, Polymer Blends, Amphiphile Phase Behavior, Molecular Modeling and Simulation, Self-Consistent Field Theory

INTRODUCTION

Exploiting molecular self-assembly is an attractive means for the production of nanostructured functional materials and is essential for miniaturization, reaching sub-2 nm feature sizes. A variety of morphologies, such as lamellae (LAM), hexagonally-packed cylinders (CYL), body-centered cubic micellar (BCC), and three-dimensional network (NET) structures, can be formed by self-assembly of amphiphilic block oligomers and related block polymers. Among these possible structures, NET structures with their bicontinuous and interconnected domains are promising for applications as nanoporous membranes,[1−3] ion transport media,[4,5] drug delivery devices,[6,7] and in many other specialty applications.[8−11] However, packing frustration often leads to a narrow composition window for stable NET phases, since the negative Gaussian curvatures of the NET connectors differ profoundly from those found within the struts, whereas the simpler LAM and CYL phases exhibit a constant mean curvature.[12] Various strategies have been introduced to drive the stable NET structures over wider composition and/or temperature ranges, including the design of amphiphiles with shape-filling architectures among ABC triblock polymers,[13] coil−brush/bottlebrush polymers,[14−18] and glycolipids,[19−21] or by addition of solvent to relieve packing frustration.[22,23]

There is also strong interest in miniaturization of the self-assembled NET feature sizes down to sub-2 nm for applications such as nanofiltration and nanopatterning.[24−27] In diblock polymer systems, microphase segregation in the mean-field limit requires the product of the chain length (N) and Flory−Huggins interaction parameter (χ) to be greater than 10.5 (for the LAM morphology), and successful efforts have been made to prepare "high χ−low N" materials with reduced domain sizes.[28−37] For example, NET phases with sub-5 nm domain spacing are observed in glycolipids and T-shaped liquid crystals.[38−42] In our previous simulation and experimental studies, a series of block oligomers containing sugar-based (A) and hydrocarbon-based (B) blocks were found to self-assemble into ordered thermotropic phases including LAM, perforated lamellae (PL), and CYL with domain periods as small as 1.2 nm,[43−45] and good agreement is observed for the domain spacing with experimental data.[44,46]

Blending or mixing block polymers has been extensively studied to create new morphologies that are absent in neat systems.[47−52] In the present study, molecular dynamics (MD) simulations are utilized to investigate blends of two block oligomers containing a hydrophilic tetraol headgroup (with four CHOH repeat units, abbreviated here as H_4) covalently connected to one or two hydrophobic alkyl tails (with CH, CH_2, and CH_3 units, abbreviated here as T): H_4T_9 and $H_4T(T_8)_2$ (Figure 1). Individually, these two molecules can
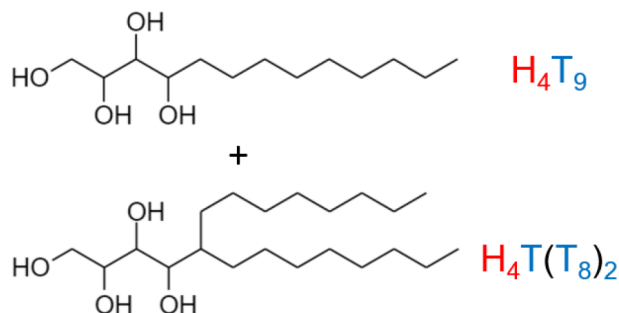

Figure 1. Chemical structures of the diblock AB (*n*-tridecan-1,2,3,4-tetraol) and triblock AB_2 (5-octyl-tridecan-1,2,3,4-tetraol) amphiphiles.

self-assemble into thermotropic liquid crystalline LAM and CYL structures, respectively.[43,45] We also perform self-consistent mean field theory (SCFT) calculations on blends of AB diblock and AB_2 miktoarm triblock polymers (with $N_A = N_B$ for both architectures) to explore the difference between the entropy-driven self-assembly of flexible block polymer blends and the enthalpy-driven self-assembly of stiff high-χ block oligomer blends.

■ RESULTS AND DISCUSSION

Phase Behavior of AB/AB$_2$ Blends

The H_4T_9 and $H_4T(T_8)_2$ blends are probed by MD simulations at $T_{SIM} = 460$ K, a temperature that is near the middle of the stability windows for the LAM and CYL morphologies formed by the neat compounds, respectively. A sequential simulation workflow is employed to deduce the appropriate system size (i.e., numbers of AB and AB_2 amphiphiles) and to set up guiding fields so that the stability of different network phases can be evaluated (see Methods section). Conceptually, the H_4T_9 and $H_4T(T_8)_2$ amphiphiles are comprised of either a ditopic or a tritopic central linker bead that is connected to a hydrophilic block comprised of four CHOH repeat units and either one or two lipophilic blocks comprised of four C_2H_4 repeat units. With identical
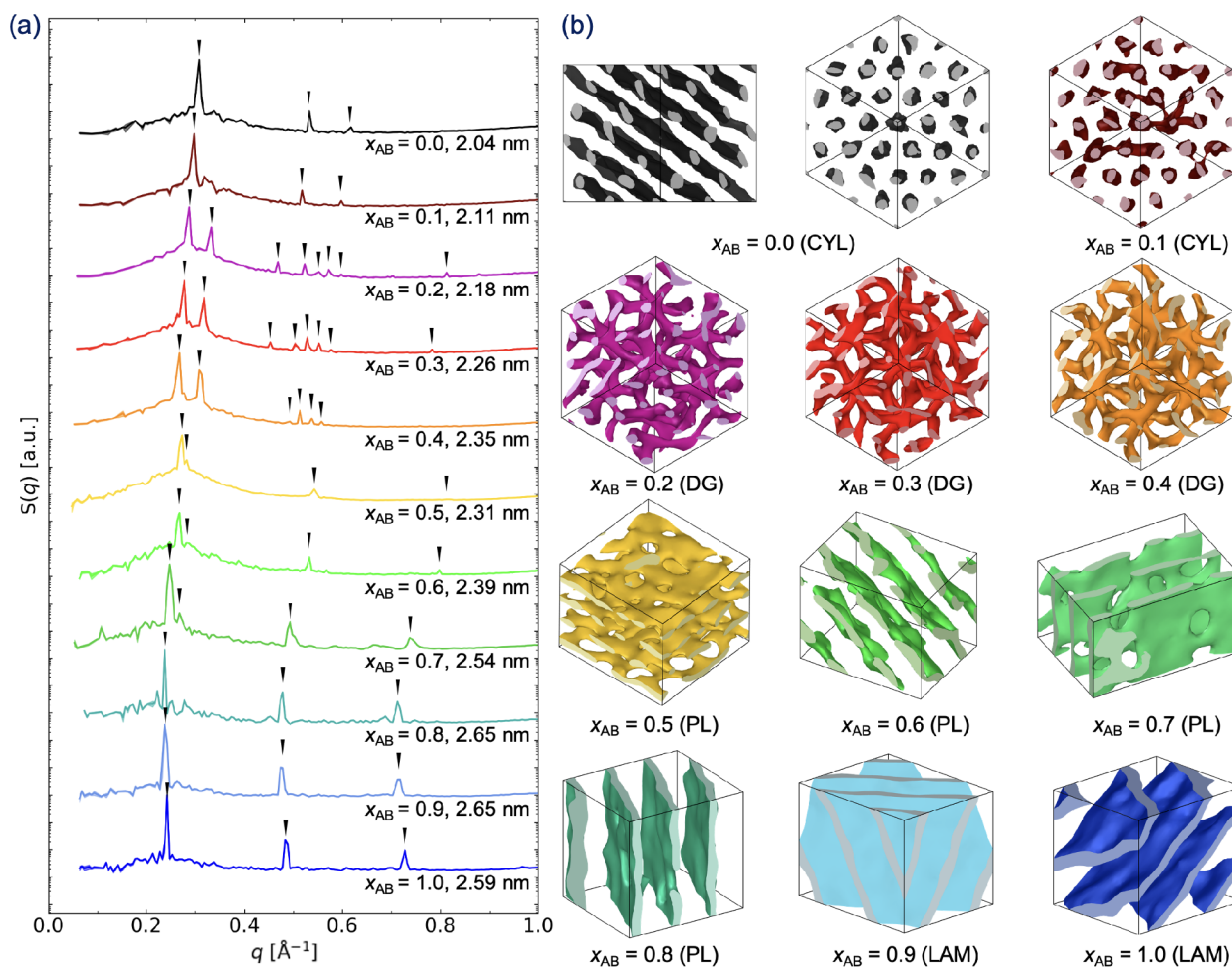
Figure 2. (a) Static structure factors $S(q)$ and (b) snapshots (only the minority block volume is shown as a surface mesh) for the equilibrium morphologies observed at $T_{SIM} = 460$ K for the different compositions (with two orientations shown for the neat AB_2 system, $x_{AB} = 0.0$). The labels denote the composition, ordered morphology, and *d*-spacing (d_{10}, d_{211}, d_{10}, and d_{10} for CYL, DG, PL, and LAM, respectively).

characteristic dimensions of A and individual B blocks, the volume fractions of the polar block (f_A) are 0.213 and 0.338 for neat $H_4T(T_8)_2$ and H_4T_9 amphiphiles, respectively. As can be observed from the static structure factors (see Figure 2; details of the calculation of the structure are provided in the Supporting Information), the neat $H_4T(T_8)_2$ system (x_{AB} = 0.0, the mole fraction of the AB amphiphile in AB/AB$_2$ blends) yields an ordered CYL phase with the characteristic structure factor peaks with q/q^* ratios of $\sqrt{1}$, $\sqrt{3}$, and $\sqrt{4}$ (where q and q^* are the magnitude of the scattering wave vector and the location of the first peak, respectively), and the d_{10}-spacing is found to be 2.04 nm. The neat H_4T_9 system (x_{AB} = 1.0) self-assembles into an ordered LAM phase with q/q^* = 1, 2, 3, ... and d = 2.59 nm from the computed structure factor. These morphologies are also evident in snapshots of the simulated systems showing the dividing surfaces between polar and nonpolar regions (see Figure 2) and the molecular configurations in ball-and-stick representations (see Figure S1 in the Supporting Information).

When only a small fraction of the other component is added to the predominantly $H_4T(T_8)_2$ or H_4T_9 systems (i.e., x_{AB} = 0.1 and 0.9), the morphologies remain unaltered relative to the neat systems (see Figure 2), but a small degree of disorder is evident in the snapshot for x_{AB} = 0.1 where "bridges" are present between some of the cylinders. At intermediate compositions, however, stable double gyroid (DG) structures are observed for x_{AB} = 0.2, 0.3, and 0.4 with the d_{211}-spacing increasing from 2.18 to 2.35 nm as more of the AB diblock is added. The characteristic peak position ratios at $\sqrt{6}$, $\sqrt{8}$, $\sqrt{16}$, $\sqrt{20}$, $\sqrt{22}$, $\sqrt{24}$, $\sqrt{26}$, and $\sqrt{48}$, consistent with the $Ia\bar{3}d$ (Q^{230}) space group symmetry,[13] are found in the structure factors obtained at these three compositions (see Figure 2a). Furthermore, this morphology assignment is supported by representative slices from the structures at x_{AB} = 0.4 (see Figure 3e and also Figures S2e and S3e for x_{AB} = 0.2 and 0.3) demonstrating that the internal DG structure is well-preserved. The propensity for these intermediate compositions to self-assemble into a stable DG morphology is also reflected from the disorganized configurations achieved rapidly from random initial structures (see Figures 3a, S2a, and S3a), where the prevalence of 3-fold connectors rules out other NET structures with 4-fold connectors (e.g., double diamond (DD), $Pn\bar{3}m$, Q^{224}) and 6-fold connectors (e.g., Plumber's nightmare (P), also referred to as double primitive, $Im\bar{3}m$, Q^{229}). Furthermore, single gyroid and double diamond structures generated through system-size tuning and guiding fields for the mixtures at x_{AB} = 0.2 to 0.4 are found to be rather unstable and turn into disordered structures within 10 ns after switching off the guiding fields (see Figure S4).

For x_{AB} = 0.5 to 0.8, self-assembly into perforated lamellae (PL) is observed. The extra peaks in the structure factors that are very close to q^* (see Figure 2a for x_{AB} = 0.5 to 0.7) reflect the average lateral domain periods between neighboring perforations. Notably, the extent of perforations increases with increasing AB$_2$ content (see Figure 2b) to allow for higher overall interfacial curvature, as the shape-filling architecture of AB$_2$ by itself favors the formation of a CYL phase. When the density of perforations is high, they can arrange into hexagonally ordered patterns. Together with the order transverse to the lamellae, the hexagonal order in the perforations imparts three-dimensional periodicity, just like NET and BCC structures, and requires system size tuning to
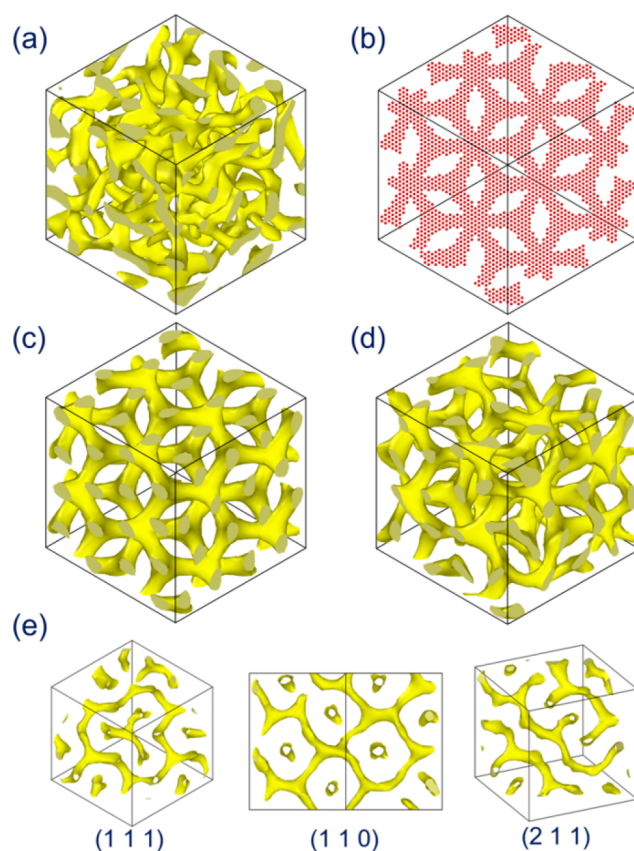

Figure 3. Snapshots of the minority-region surface meshes at x_{AB} = 0.4 and T_{SIM} = 460 K for (a) a nonequilibrium, disordered bicontinuous structure with system size fine-tuned for a DG structure with 8 unit cells. (b) Interaction sites residing in the subvolume of a DG network that are used as the guiding field to aid the self-assembly process. (c) Equilibrium structure under the applied guiding field. (d) Equilibrium structure reached after the guiding field is removed. (e) Slices with thickness of 15 Å in (111), (110), and (211) directions of the equilibrated DG structure without guiding field.

achieve ordered abab... (HPL$_{ab}$) and abcabc... (HPL$_{abc}$) stackings. Because of the prohibitively large unit cell dimensions, fine-tuning of system sizes to achieve the HPL morphology[45] is not attempted, and these morphologies are referred to as PL throughout this work. Prior work on diblock polymer melts showed two additional peaks for hexagonally perforated layers (HPL),[53] but our previous simulations for linear BAB triblock oligomers also yield a single additional peak for a well-ordered HPL morphology.[45] Thus, it is possible that the different packing constraints for the stiff oligomers lead to a close match of lamellar spacing and perforation distance resulting in one of the minor peaks being hidden within the main peak.

To test that the PL structure for the mixture at x_{AB} = 0.5 is stable, system-size tuning and guiding field are applied to generate a DG structure. However, we observe (see Figure S5) that, upon removal of the guiding field, the system rapidly evolves over only 10 ns into a disordered bicontinuous structure with flatter (i.e., less spherical) cross-sections of the struts than found for the DG structure at x_{AB} = 0.4. After a much longer trajectory (≈800 ns), a PL-like morphology is recovered for this simulation at x_{AB} = 0.5.

A convolutional neural network for image recognition in Fourier space (FTCNN, see Methods) designed to distinguish
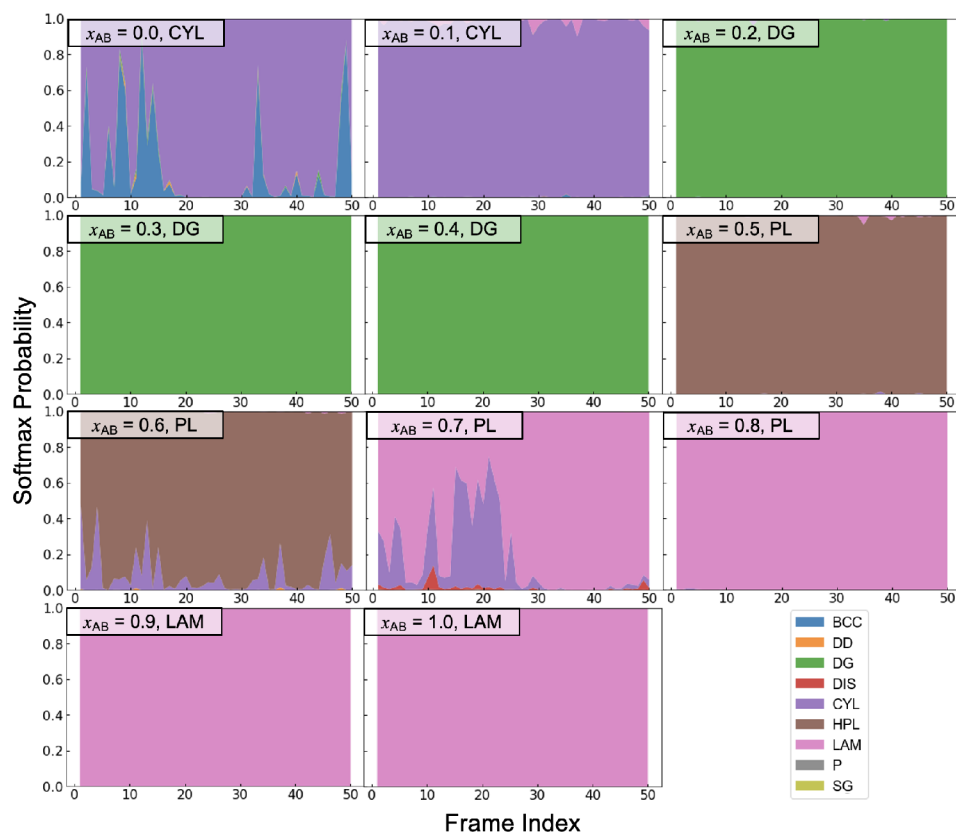
Figure 4. Stack plots of the softmax classification probabilities obtained from the Fourier transform convolutional neural network (FTCNN) model for all compositions. For each x_{AB}, 50 simulation frames separated by 2 ns are selected for inference: body-centered cubic micelles (BCC), double diamond (DD), double gyroid (DG), disordered (DIS), hexagonally packed cylinders (CYL), hexagonally perforated lamellar (HPL), lamellar (LAM), plumber's nightmare (P), and single gyroid (SG).

various ordered morphologies and trained on ordered and disordered structures of diblock oligomers and of star triblock oligomers (but not including any blends and only synthetic data for network morphologies)[54] also distinguishes among the PL structures (see Figure 4). It should be noted that the PL morphology with disordered perforations was not included as a class during the FTCNN training. For the mixtures at $x_{AB} = 0.5$ and 0.6 with their high density of perforations, the FTCNN classifies individual configurations encountered through the trajectory as HPL (see Figure 4), whereas the configurations for $x_{AB} = 0.7$ and 0.8 with low densities of perforations are classified as LAM. A small fraction of the configurations for the $x_{AB} = 0.7$ mixture are misclassified as CYL. The configurations from the mixtures at $x_{AB} = 0.0$ and 0.1 are classified overwhelmingly as CYL with the occasional misclassification as body-centered cubic micelles. Every configuration for the mixtures at $x_{AB} = 0.2$, 0.3, and 0.4 is classified as DG, and zero probabilities are assigned to the other three types of canonical network phases in the training set, thereby providing further support for the stability of the DG morphology. Similarly, the configurations for the mixtures at $x_{AB} = 0.2$, 0.3, and 0.4 are with a very high degree of certainty classified as LAM.

Domain Spacing and Amphiphile Packing

Although the lengths of the A and B blocks in the H_4T_9 and $H_4T(T_8)_2$ amphiphiles are matched, the domain spacing ($d = 2\pi/q^*$) varies considerably among the ordered structures. A plot of the domain spacing as a function of x_{AB} (see Figure S6) indicates an approximately linear increase with $(\partial d/\partial x_{AB})_{p,T} = 0.08$ nm for $x_{AB} \leq 0.4$ covering the CYL and DG

morphologies. Similarly, we find an approximately linear increase but with larger $(\partial d/\partial x_{AB})_{p,T} = 0.11$ nm for the PL region ($0.5 \leq x_{AB} \leq 0.8$). The transition from DG to PL morphology ($x_{AB} = 0.4$ and 0.5, respectively) leads to a discontinuous drop in d by ≈ 0.1 nm. Interestingly, $d = 2.65$ nm is found for both the PL structure at $x_{AB} = 0.8$ and the LAM structure at $x_{AB} = 0.9$, and d actually appears to decrease as the AB_2 molecules are removed to reach the neat AB system. For the CYL morphology, the d_{10} spacing corresponds to the distance between rows of cylinders and not to the distance between the cylinders. The radial distribution function (RDF) for the terminal oxygen atoms (i.e., primary hydroxyl groups) of the H_4T_9 and $H_4T(T_8)_2$ amphiphiles is another metric to probe the spacing between the minority blocks (see Figure S7). The broad fourth peak represents the head-to-head spacing between two domains. There is a clear trend of the fourth peak position shifting toward larger values with increasing x_{AB}. The positions of the fourth peak are approximately 20% larger than the d-spacings, indicating that the primary hydroxyl group is not anchored to the center of the polar domain. As an aside, the lower height of the fourth peak for for $x_{AB} = 0.1$ reflects the disorder introduced by bridges between the cylinders (see Figures 2b and S1).

The contour length of an H_4T_9 amphiphile is ≈ 1.9 nm, which is considerably larger than $d/2 = 1.3$ nm and the 1.6 nm deduced from the fourth peak position of the LAM phases. The simulation snapshots (see Figure S1) illustrate a significant degree of interdigitation of the lipophilic tails for the CYL morphology (where even the center of the triangular

space between three neighboring cylinders shows relatively high occupancy by tail segments. Only the amphiphiles in the simulation box are shown, and thus, the central part of the tilted box gives the best impression of the packing, whereas periodic images would be needed toward the edges) and also for the PL phases with $x_{AB} \leq 0.7$ (where the central region between two polar sheets also shows high occupancy). In contrast, the snapshots for the PL morphology at $x_{AB} = 0.8$ and for the LAM morphology clearly indicate a region of low density at the midpoint between the leaflets; i.e., there is less interdigitation. The cross-section of the "branched" headgroup with its CHOH repeat units is larger than that of a single nonpolar tail but smaller than that occupied by two tails. Thus, a higher degree of tilt of the nonpolar tails away from the direction normal to the lamellar plane is needed as the fraction of AB_2 amphiphiles is reduced, thereby explaining the small decrease in d_{10} observed for $x_{AB} = 0.9$ and 1.0.

Since the AB and AB_2 amphiphiles share a common tetraol (H_4) headgroup, we focus on the packing of the tail groups that occupy a volume fraction of about 75%. Specifically, we surmise that differences in the shape of the T_9 and $T(T_8)_2$ tail groups reflected in the orientational distributions of neighboring alkyl tails lead to different preferred local interfacial curvature between the A-rich and B-rich regions. Here, we define this interface through the positions of "junction" beads, J, placed at the center of the C−C bond connecting the H and T segments. Analysis of the J−J RDF (see Figure S8) shows remarkably consistent features for all compositions (despite their different morphologies) with the first peak and minimum located at 5.5 and 7 Å, respectively; 7 Å is used as the distance cutoff to define the first coordination sphere of a J bead (see Figure 5b). The orientation of an alkyl tail is then determined by the vector $\vec{R}_{AB}$ or $\vec{R}_{AB_2}$ that points from J to each terminal methyl group (see Figure 5a). The angle θ measures the relative alignment of two alkyl tail vectors belonging to two amphiphiles with neighboring J beads; AB−AB, AB−AB_2, and AB_2−AB_2 pairs yield one, two, and four distinct θ angles, respectively.

Angular distribution functions (ADF) for tail group end-to-end vectors belonging to neighboring J beads are shown in Figure 5c (see also Figure S9 for the corresponding heatmap). The ADFs fall into four groups with distinct features. For the LAM phases formed at $x_{AB} = 1.0$ and 0.9, parallel orientations ($\theta = 0°$) are strongly preferred, angles between 90 and 150° are least favorable, and a small fraction of neighboring vectors are found with antiparallel orientation. Given the tight cutoff distance of 7 Å, the antiparallel orientations arise mostly from AB molecules with their A segments in the same sheet and their tails pointing into different nonpolar regions of the LAM phase. At $x_{AB} = 0.8$ and 0.7, the PL phases with a low density of perforations show a weaker preference for parallel orientations, but a minimum and a secondary maximum in the ADF are now observed for $\theta \approx 40$ and 50°, respectively. Marked changes are evident for the transition to PL phases with a high density of perforations ($x_{AB} = 0.6$ and 0.5); here, the ADFs are approximately symmetric with a preference for angles between 50 and 130°.

The ADFs for the systems with DG morphology ($x_{AB} = 0.4$ to 0.2) fall in between those of the PL phases with low and high densities of perforations. That is, angles with $\theta < 90°$ are clearly preferred over those with $\theta > 90°$ (i.e., the ADFs are far from symmetric), angles near 50° are now most preferred, and
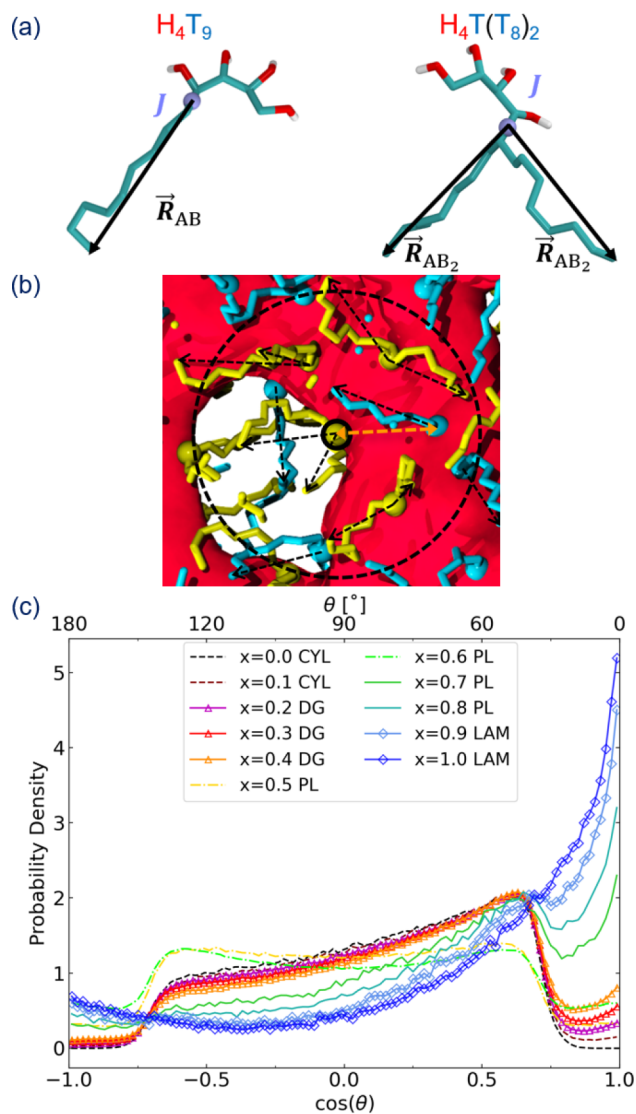
Figure 5. (a) Illustration of the junction sites J and $\vec{R}_{AB}$ and $\vec{R}_{AB_2}$ vectors for the diblock and triblock amphiphiles. (b) Zoomed-in snapshot of a perforation for the PL structure at $x_{AB} = 0.6$. The minority (polar) region is shown as red surface mesh, and the nonpolar segments of AB and AB_2 amphiphiles are displayed in cyan and yellow, respectively. A spherical region with radius of 7 Å centered at one junction is indicated by the dashed line. (c) Angular distribution functions for the tail group end-to-end vectors from neighboring J sites for all compositions (x_{AB}) at $T_{SIM} = 460$ K.

there is only a weak secondary maximum for parallel orientations. This secondary maximum gradually becomes weaker for the DG phases as x_{AB} decreases and is no longer present for the CYL phase containing only AB_2 amphiphiles. Interestingly, as x_{AB} decreases, the population for angles up to 130° increases, whereas the fraction of antiparallel orientations decreases. These subtle changes are likely caused by the cross-section of the polar cores of the cylinders and circular struts possessing a diameter that is slightly larger than the thickness of the polar regions with low curvature forming the nodes and lamellar sheets.[55] Figures S10−S12 show 2-D radial-angular distribution functions (RADFs). When accounting for the increase in volume for radial shells (i.e., distance-normalized), then the strongest orientational preferences are observed for J−J distances, r_{JJ}, near 5.5 Å, the location of the maximum in

the RDFs. The RADFs also show that the antiparallel orientations found for the LAM phases are associated with larger r_{JJ} values near the distance cutoff. The fairly sharp boundaries for $|\cos\theta| > 0.8$ observed for the CYL phases can be attributed to the double tails of the AB_2 amphiphiles where a pair of neighboring J beads results in the calculations of four angles that are constrained by the preference for certain intramolecular conformations.

The angular distribution for the intramolecular CH_3-J-CH_3 angle of the AB_2 amphiphiles is also analyzed to assess whether changes in self-assembly morphology are accompanied by changes in the molecular shape. Despite the short length of the alkyl tails, the CH_3-J-CH_3 distribution is broad with a weak preference for angles near 100° and a shoulder near 20° for $x_{AB} \leq 0.6$ (see Figure S13). As the morphology transitions to PL with low density of perforations and LAM ($x_{AB} \geq 0.7$), the distribution shifts toward angles between 20° and 80° that allow for better packing in these low-curvature morphologies.

## Local Composition Enhancement

For a blend, an important question is whether a network morphology containing nodes and struts with nonconstant Gaussian interfacial curvature can be stabilized by local segregation of the different shape-filling amphiphiles. In the DG morphology, the minority domain consists of two opposite-handed, interpenetrating node-strut networks formed by the polar A blocks, while the majority B blocks fill the remaining space. For the simulation box containing 2^3 unit cells, we define spherical subvolumes (Figure 6a) with a radius of r_{cut} around the centers of all 128 nodes (each DG unit cell contains 16 equivalent node positions according to the $Ia\bar{3}d$ symmetry). The local mole fraction within a given subvolume is then calculated as $x_{O,AB}^{node}(r_{cut}) = N_{O,AB}(r_{cut})/[N_{O,AB}(r_{cut}) + N_{AB_2}(r_{cut})]$, where $N_O(r_{cut})$ is the number of oxygen atoms within the subvolume belonging to a given type of amphiphile. Some caution is required for the choice of the subvolume. When r_{cut} is too small, it does not cover all of the node region and small N_O values lead to large statistical uncertainties. When r_{cut} is set to half of the distance between two neighboring nodes, $d_{node} = a/2^{3/2}$ (where a is the length of the cubic unit cell), then the spherical subvolumes of adjacent nodes will touch and higher r_{cut} values are not appropriate. For the AB/AB_2 blends investigated here, d_{node} ranges from 1.89 nm ($x_{AB} = 0.2$) to 2.03 nm ($x_{AB} = 0.4$). As shown in Figure 6b, the local composition in the vicinity of the node locations is enhanced in polar groups from the AB amphiphiles compared to the global mole fraction, x_{AB}. The enhancement is larger for the blend with $x_{AB} = 0.4$ than for $x_{AB} = 0.2$ and diminishes with increasing r_{cut}. It should be noted here that only a small subregion at the node center is characterized by a flat interface with zero normal curvature, whereas the node edges between the struts possess high normal curvature and negative Gaussian curvature. Nevertheless, there is clear indication that the DG morphology is stabilized by a significant degree of local segregation. Local segregation has also been observed in SCFT calculations for blends of a gyroid-forming diblock polymer and a homopolymer-like diblock polymer, where the latter is enriched at the node.[56]
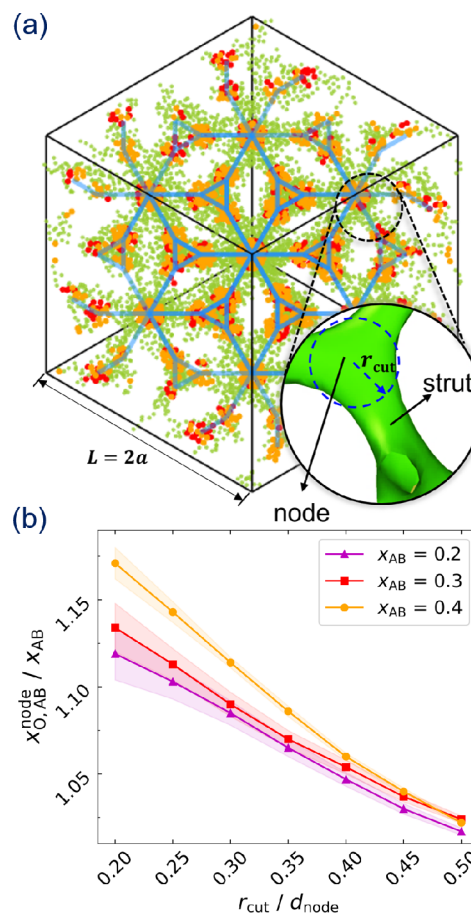
Figure 6. (a) Snapshot of the DG structure at $x_{AB} = 0.3$. The red and orange dots highlight oxygen atoms from AB and AB_2 amphiphiles, respectively, that are found within spherical subvolumes centered at all the node locations with a radius equivalent to a quarter of the distance between adjacent nodes ($r_{cut} = d_{node}/4$). The remaining oxygen atoms are displayed as green dots. Blue lines represent the DG skeleton. The zoomed-in area shows the surface mesh of a node and connecting strut. The simulation box contains eight unit cells. (b) Local composition enhancement for oxygen atoms of AB amphiphiles in nodal subvolumes ($x_{O,AB}^{node}/x_{AB}$) as a function of cutoff distance. The shaded areas represent the 95% confidence intervals.

Phase Behavior of AB and AB_2 Block Polymer Blends from SCFT Calculations

A comparison of the phase diagrams for the AB/AB_2 amphiphile (from MD simulations) and block polymer (from SCFT calculations) blends is shown in Figure 7. The most striking difference between these two systems is the absence of a PL phase in the block polymers (with $N_A = N_B$ for each block; i.e., $f_A = 0.5$ and 0.333 for the diblock and star polymers, respectively). For the block polymer mixture, it is not surprising that the HPL phase is absent when the perforated lamellar structures are comprised of the A blocks. For pure diblock polymer melts, HPL is metastable due to the high packing frustration in the majority component domain;[12] the addition of majority-component homopolymers is predicted to reduce this packing frustration and stabilize the HPL phase.[57,58] For AB_2 star polymer melts, SCFT predicts a narrow composition window for which the HPL morphology is stable at high segregation when B is the minority block.[59] When A is the minority block, however, the HPL phase becomes unfavorable for the AB_2 miktoarm architecture due to
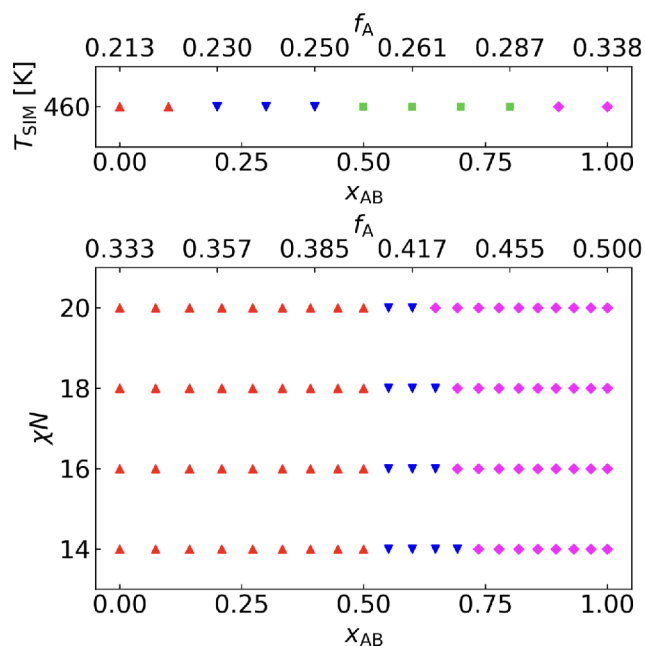
Figure 7. Phase diagrams as a function of the mole fraction for (top) AB and AB$_2$ amphiphile mixtures from MD simulations at T_{SIM} = 460 K and (bottom) AB diblock and AB$_2$ star polymer mixtures with the same statistical segment lengths from SCFT calculations at different χN values, where N is the degree of polymerization of the AB chains. CYL, DG, PL, and LAM morphologies are represented by red up triangles, blue down triangles, green squares, and magenta diamonds, respectively. The A-block volume fractions are indicated at the tops of the graphs.

the high entropic penalty of stretching the B blocks to fill the majority-component layers, which makes the HPL phase less stable than for linear diblock polymer melts. Considering the phase behavior of these two neat block polymers, we would not anticipate that mixing of AB and AB$_2$ would give rise to an HPL phase when A is the minority block. In contrast, when B is the minority block, HPL is observed at high segregation in SCFT for the AB and AB$_2$ blend system with a very small composition of the AB block polymers (see Figure S14). We thus conclude that the presence of PL in the block oligomer system is enthalpically driven since the entropic chain stretching penalties, which drive the frustration in the block polymer system and suppress PL, are less important for the stiff oligomers.

We also observe that the gyroid region for the block polymers is shifted to higher f_A values compared to the block oligomer blends. In the block polymer system, the geometry of the microstructure is determined by a competition between the stretching penalties of the A and B blocks, balanced by the unfavorable energy associated with the interfacial area between the A-rich and the B-rich domains. For example, as the block composition of a diblock polymer becomes more asymmetric, a more curved geometry is preferred to minimize the total stretching energy.[60] Moreover, architecturally asymmetric miktoarm star block polymers spontaneously curve toward the minority domains.[61,62] Since the chain stretching entropy is an essential thermodynamic factor for the high-molecular-weight block polymer systems, the gyroid region positioned at relatively higher x_{AB} (and f_A) values can be rationalized by the spontaneous curvatures induced by the entropic driving force in the asymmetric polymer architectures, but the directional

character of the strong hydrogen-bond interactions and the slight bottlebrush character present for the minority component of the amphiphiles certainly also plays a role. In the mean-field limit, the relative strength of the A−A and B−B interactions ($\varepsilon_{AA} - \varepsilon_{BB}$) does not directly impact the selection of the ordered state because the free energy term reflecting the difference in the self-interaction energies alters the free energies of all morphologies in the same way at a given volume fraction of A-monomers. However, the Flory−Huggins parameter χ expressed in terms of ε_{AA}, ε_{BB}, and ε_{AB} increases with increasing ($\varepsilon_{AA} - \varepsilon_{BB})/k_B T$, where ε_{ij} is defined as the depth of the potential energy well, so the effect of increasing relative attractive A−A interactions on selection of the ordered state is the same as the effect of increasing χ.

Comparison to Blends of AB and A(B$_2$) Diblock Oligomers and Polymers

To assess the importance of the architectural difference (i.e., diblock and miktoarm triblock) of the oligomers and polymers on the phase behavior, we also carried out MD simulations for which the branched H$_4$T(T$_8$)$_2$ amphiphile is replaced by its linear analogue H$_4$T$_{17}$ (n-heneicosan-1,2,3,4-tetraol abbreviated as A(B$_2$)). For the stiff oligomers, we observe that the LAM morphology persists for linear diblock architectures (see Figure 8) even when the volume fraction of the minority block
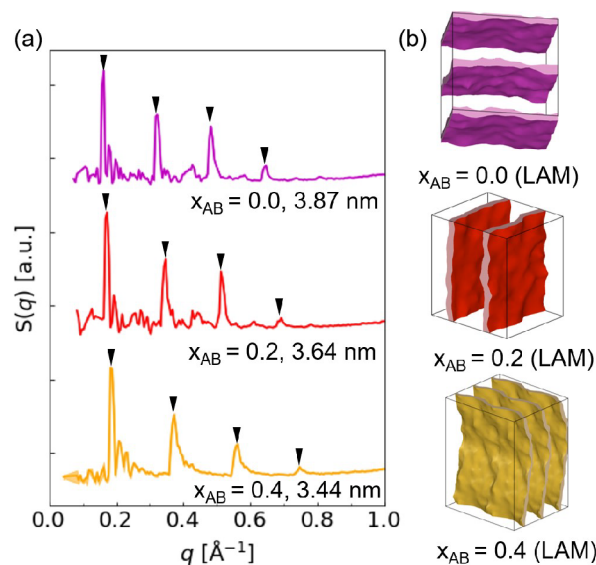
Figure 8. (a) Static structure factors $S(q)$ and (b) snapshots (only the minority block volume is shown as a surface mesh) for the equilibrium morphologies observed at T_{SIM} = 460 K for AB/A(B$_2$) diblock blends for $x_{AB} \leq 0.4$. The labels denote the composition, ordered morphology, and d_{10}-spacing.

is lowered. As should be expected, increasing x_{AB} results in a decrease of the domain spacing as a longer linear amphiphile is replaced with a shorter one.

Data for the analogous SCFT calculations considering blends of an AB diblock polymer (f_A = 0.5) and a 1.5 times longer A(B$_2$) diblock polymer (f_A = 0.333) are shown in Figure S15. Compared to the AB/AB$_2$ blend, the stability window for the LAM morphology for the diblock AB/A(B$_2$) blend is significantly extended down to $x_{AB} \approx 0.2$, and the DG window is shifted to the A(B$_2$)-rich region. For the neat A(B$_2$) diblock polymer, the CYL morphology is stable for low χN values, whereas DG is found for high χN values, and the results

are consistent with the phase behavior predicted for a neat diblock polymer with $f_A = 0.333$.[56] Different binary blends of linear AB diblock copolymers have been examined previously by SCFT calculations, and Lai and Shi[56] predicted the formation of a double diamond phase for the binary mixture where one species is a homopolymer-like AB diblock. Their calculations illustrate that for diblock polymer mixture systems, the relative block composition plays an essential role in manipulating the stabilization of network morphologies.

CONCLUSION

MD simulations are utilized to probe the phase behavior for blends of low-molecular-weight AB diblock and AB_2 miktoarm triblock amphiphiles containing polar, sugar-based (A) and nonpolar, hydrocarbon (B) segments. In their pure form, the AB and AB_2 amphiphiles are capable of self-assembling into ordered LAM and CYL phases, respectively. Blending these two amphiphiles gives rise to large composition windows for stable DG networks and PL phases. Sub-3 nm d-spacings (or the included sphere for the B-region in DG) are achieved for all ordered morphologies. The different ordered morphologies are enabled due to the propensities of AB and AB_2 amphiphiles for different B block orientational alignments and local demixing that, for example, yields a slightly enhanced fraction of AB amphiphiles in the nodes of the DG network. SCFT calculations for AB and AB_2 block polymer blends also yield a window for a stable DG phase, yet a stable PL region is not observed when A is the minority block. This work illustrates the differences and similarities between diblock/triblock polymer mixtures and stiff/H-bonding oligomer mixtures and points to the need for adjustments of the design principles for tuning shape-filling oligomer/polymer architectures to achieve wide stability windows for network phases that provide domain sizes ranging from a few to many tens of nanometers.

METHODS

Molecular Models and Simulation Details

The transferable potentials for phase equilibria united-atom (TraPPE-UA) force field is used to model the H_4T_9 and $H_4T(T_8)_2$ amphiphiles (see Supporting Information and Tables S1 and S2 for force field details). Molecular dynamics (MD) simulations are performed in the isobaric−isothermal (NpT) ensemble using the GROMACS 2021.3 software.[63,64] The system sizes range from 1000 to 2000 molecules. The Nosé−Hoover thermostat[65,66] with a time constant $\tau_T = 0.4$ ps and the Parrinello−Rahman barostat[67] with a time constant $\tau_p = 2$ ps are used to control temperature and pressure, respectively. The particle-mesh Ewald method[68] is used to compute the electrostatic interactions. The p-LINCS algorithm is used to constrain the O−H bond length,[69] which enables a 2 fs time steps. The initial disordered configurations used as input for the MD simulations are generated from short Monte Carlo (MC) simulations in the canonical ensemble ($T_{SIM} = 3000$ K). The simulated systems contain random mixtures of stereoisomers for each amphiphile because the coupled-decoupled configurational-bias MC moves[70] applied to a united-atom model do not preserve the tacticity (whereas specific synthesis routes may yield a preference for specific stereoisomers[44]). MD trajectories consisting of at least 300 ns are used to equilibrate the systems at $T_{SIM} = 460$ K. Thereafter, trajectories of an additional 100 ns for LAM, PL, and CYL phases and of 600 ns for DG phases are performed and used for the structural analysis. Logarithmic plots of the mean-squared displacements obtained during the analysis period indicate that the AB and AB_2 molecules reach the diffusive regime beyond 200 ns, and the amphiphiles diffuse on average by more than twice the domain spacing over 600 ns (see Figure S16). The simulation snapshots

showing surface meshes and ball-and-stick representations are produced with the Ovito and VMD visualization packages.[71,72]

System Size Tuning and Workflow

For all the x_{AB} values, initial simulations for 1000-molecule systems utilize orthorhombic simulation cells to allow for independent fluctuations in x-, y-, and z- dimensions to ameliorate incommensurability effects.[73,74] However, this strategy is only suitable for morphologies with periodicity in one or two dimensions, such as the LAM and CYL morphologies. In this case, the segregated domains can reach the preferred domain spacing through rotations, lateral expansions, or contractions in the perpendicular direction to the planes of lamellae or the axes of cylinders.

For the 1000-molecule systems at x_{AB} values of 0.2, 0.3, and 0.4, locally segregated but globally disorganized networks are observed. Such defective NET structures are expected, because for three-dimensionally periodic structures, such as BCC and NET, the commensurability issue persists unless the simulation box contains exactly integer multiples of the unit cell which requires knowledge of the lattice parameter (a) and the number of molecules per unit cell (N_{UC}). In addition, the structural orientation must match, or the system is likely to end up with distorted and metastable structures induced by the simulation box, which are unstable in the thermodynamic limit.[75−77] Thus, the system size has to be optimized for these structures. To fine-tune the simulation box so that it contains integer multiples of unit cells with accurate a and N_{UC} that corresponds to a specific periodic structure, the structure factor, $S(q)$, for the disorganized NET-like structures is first calculated, and the appropriate unit cell dimensions for a specific morphology (assuming cubic) is estimated using the position of the broad peak:[78] $a = 2\pi m/q^*$ where m corresponds to the first observable reflection spacing ratio of that morphology (e.g., $m = \sqrt{2^2 + 1^2 + 1^2} = \sqrt{6}$ for DG). The N_{UC} can now be estimated using the average volume per molecule from the initial simulation. For each x_{AB} forming a disorganized NET structure, the simulations were reinitiated with $8N_{UC}$ molecules estimated for NET phases including double gyroid (DG), double diamond (DD), and single gyroid (SG) structures, within a cubic simulation box of length $L_{box} = 2a$. However, even with a reasonable system size, equilibrating the system into one of the ordered NET structures is still challenging due to the small free energy difference between the disorganized and ordered NET phases.[76] Therefore, we utilize a MD workflow for 3D NET simulation,[79] which employs a guiding field generated by Gaussian interaction sites of different strengths for H and T beads that uniformly reside in the minority and majority domains of the candidate NET structures. For example, Figure 3b shows the guiding sites for the minority domain of a DG structure containing 8 unit cells. With the presence of the guiding field, the A and B blocks are aligned into two different domains of the ordered gyroid matrices (e.g., Figure 3c). Then the guiding field is removed, and the stability of each candidate NET morphology is assessed over a prolonged trajectory of $\approx 1\ \mu$s (e.g., see Figure 3d,e). The values of N_{UC} and other details of the DG unit cells are reported in Tables S3 and S4.

Fourier Transform Convolutional Neural Network

The FTCNN is a three-dimensional convolutional neural network (CNN) that encodes representations of the discrete volumes to extract more discriminative features of each sample. For the training, we use the same point cloud data as in our previous work of a PointNet,[54] a deep neural network for simulation morphology detection using point clouds. These point clouds contain the coordinates representing repeat units of the minority component for nine distinct morphologies: body-centered cubic micelles, double diamond, double gyroid, disordered, hexagonally packed cylinders, hexagonally perforated lamellar, lamellar, plumber's nightmare, and single gyroid. To ensure the rotational invariance for the classification results, a spatially uniform random rotation was applied on each point cloud, and the resulting point cloud was wrapped into the original box using the periodic boundary condition. All rotated point clouds were then voxelized into $16 \times 16 \times 16$ volumetric occupancy grids (see
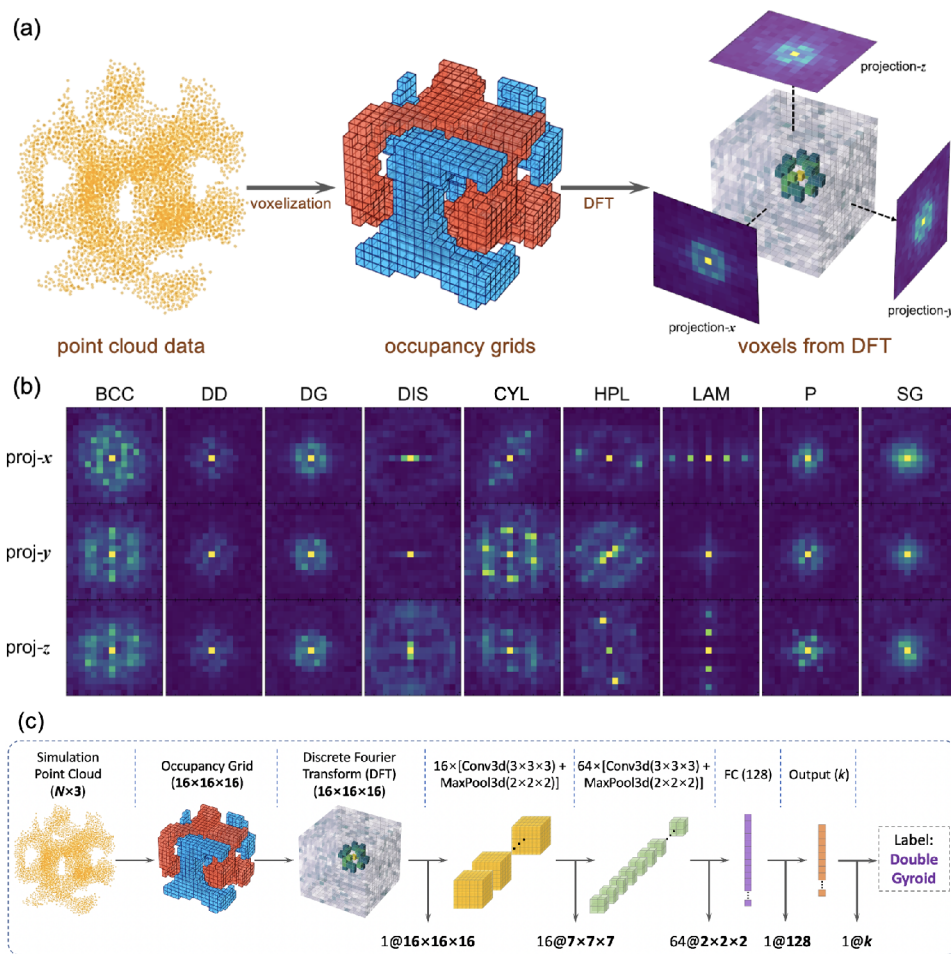
Figure 9. (a) Process of generating the voxel training set data (16 × 16 × 16) from a sample point cloud taken from a synthetic double gyroid structure. (b) Projections of the Fourier transformed 3-D occupancy grids (16 × 16 × 16) in x-, y-, and z-directions represented as heatmaps. (c) Schematics of the FTCNN network, including the data preprocessing stage. The 3-D voxels obtained from discrete Fourier transform of the occupancy grids or the corresponding point clouds are fed into two 3-D convolution layers accompanied by max-pooling layers that are followed by a fully connected layer and a softmax layer for the classification task.

Figure 9a). The value in each voxel grid represents the number of points inside the corresponding cubic subregion. Then, the discrete Fourier transform is applied on voxelized point clouds as described by the following equation:

$$F(u, v, w) = \sum_{x=0}^{N_x} \sum_{y=0}^{N_y} \sum_{z=0}^{N_z} f(x, y, z) \times$$
$$\exp\left[-2\pi i \left(u\frac{x}{N_x} + v\frac{y}{N_y} + w\frac{z}{N_z}\right)\right] \tag{1}$$

where $f(x, y, z)$ denotes the values of voxel grids as a function of the grid indices; N_x, N_y, and N_z are the number of grids along x, y, and z directions; and u, v, and w are the indices in the reciprocal lattice. The fast Fourier transform algorithm[80] was used for efficient computation of $F(u, v, w)$. For consistency, the zero-frequency component is shifted to the center of each spectrum. Examples of the processed voxels and their projections in x, y, and z directions or, equivalently, $y − z$, $x − z$, and $x − y$ planes can be seen from Figure 9b. By such periodic transformation, the translational invariance of the structures under the periodic boundary conditions is ensured. Therefore, no extra preprocessing for the point clouds was required before being voxelized.

The FTCNN is built with six hierarchically stacked layers including 3D convolutional layers, 3D max-pooling layers, and fully connected layers (see Figure 9c). The input voxels are first fed into two

consecutive composite layers, each consisting of one 3D convolutional layer with a kernel size of 3 × 3 × 3 and one max-pooling layer with a 2 × 2 × 2 voxel window to down-sample the feature volumes. These two composite layers contain 16 and 64 filters, respectively. In contrast to the PointNet layers,[54,81,82] which make the prediction results invariant to the order of the input points, the convolution operation used in a CNN is index-ordered. This is because, for the Fourier transformed occupancy grids, the relative positions of the high-intensity grids are crucial to distinguish among different original structures. Subsequently, two fully connected layers with 128 and k neurons are used to output the classification labels. In this case, $k = 9$, which refers to nine distinct equilibrium morphologies. Leaky rectifed linear units (LReLU) with a slope of 0.01 for negative values were applied as activation functions after each convolutional and fully connected layer. Batch normalization and dropout with a 0.85 keep ratio are applied before the last fully connected layer. For each morphology, 3000 voxels are obtained by preprocessing the point clouds from the MD simulation trajectories and the synthetic network structures[54] and are split into training and test data in a 4:1 ratio. The model is trained over 1000 epochs with a batch size of 128 voxels. The Adam optimizer[83] is used with a learning rate of 0.001. The exponential decay rates for the first and the second moments are chosen as 0.9 and 0.999, respectively. The model is implemented in PyTorch.

SCFT Calculations

Canonical SCFT calculations for incompressible melts of AB and AB$_2$ block polymer blends ($N_A = N_B$, i.e., $f_A = 0.5$ for $x_{AB} = 1$ and $f_A = 0.33$ for $x_{AB} = 0$) are performed using the CPU version of the open-source C++ PSCF software.[84] In the SCFT calculations, both AB and AB$_2$ block polymers are modeled as flexible Gaussian chains with equal degrees of polymerization for each A and B block, $N_A = N_B$, and equal statistical segment lengths. The modified diffusion equation in SCFT[85] is numerically solved using the pseudospectral method[86] with periodic boundary conditions, integration steps of $ds = 0.01$, and spatial grid sizes of 40^3. Initial guesses for LAM, DG, and CYL are all readily available from prior work.[85] For rapid convergence of the SCFT algorithm, we generate the initial guess chemical potential fields for the perforated lamellae by a level set method,[85] which calculates the initial input structure by the level surface of the first nonzero symmetry-adapted basis function of the specific space group. The fields are then iteratively updated using an Anderson-mixing scheme, optimizing the variable unit-cell dimensions with stress relaxation.[87] The iterations are stopped when the errors in the self-consistent field equations drop below the specified tolerance of $\varepsilon = 10^{-5}$. After obtaining the self-consistent mean field solutions, the free energies of the LAM, DG, CYL, and HPL phase (with ab and abc stacking) are calculated and compared to determine the equilibrium states.

■ ASSOCIATED CONTENT

ⓈⒾ Supporting Information

The Supporting Information is available free of charge at https://pubs.acs.org/doi/10.1021/jacsau.2c00101.

> Additional force field details; details on structure factor calculation; and supplementary tables and figures (PDF)

■ AUTHOR INFORMATION

Corresponding Authors

Timothy P. Lodge − *Department of Chemical Engineering and Materials Science, University of Minnesota, Minneapolis, Minnesota 55455-0132, United States; Department of Chemistry, University of Minnesota, Minneapolis, Minnesota 55455-0431, United States;* ⓘ orcid.org/0000-0001-5916-8834; Email: lodge@umn.edu

J. Ilja Siepmann − *Department of Chemical Engineering and Materials Science, University of Minnesota, Minneapolis, Minnesota 55455-0132, United States; Department of Chemistry and Chemical Theory Center, University of Minnesota, Minneapolis, Minnesota 55455-0431, United States;* ⓘ orcid.org/0000-0003-2534-4507; Email: siepmann@umn.edu

Authors

Zhengyuan Shen − *Department of Chemical Engineering and Materials Science, University of Minnesota, Minneapolis, Minnesota 55455-0132, United States; Chemical Theory Center, University of Minnesota, Minneapolis, Minnesota 55455-0431, United States*

Ke Luo − *Department of Chemistry and Chemical Theory Center, University of Minnesota, Minneapolis, Minnesota 55455-0431, United States*

So Jung Park − *Department of Chemical Engineering and Materials Science, University of Minnesota, Minneapolis, Minnesota 55455-0132, United States;* ⓘ orcid.org/0000-0002-3003-6501

Daoyuan Li − *Department of Chemical Engineering and Materials Science, University of Minnesota, Minneapolis, Minnesota 55455-0132, United States; Chemical Theory*

Center, University of Minnesota, Minneapolis, Minnesota 55455-0431, United States

Mahesh K. Mahanthappa − *Department of Chemical Engineering and Materials Science, University of Minnesota, Minneapolis, Minnesota 55455-0132, United States;* ⓘ orcid.org/0000-0002-9871-804X

Frank S. Bates − *Department of Chemical Engineering and Materials Science, University of Minnesota, Minneapolis, Minnesota 55455-0132, United States;* ⓘ orcid.org/0000-0003-3977-1278

Kevin D. Dorfman − *Department of Chemical Engineering and Materials Science, University of Minnesota, Minneapolis, Minnesota 55455-0132, United States;* ⓘ orcid.org/0000-0003-0065-5157

Complete contact information is available at:
https://pubs.acs.org/10.1021/jacsau.2c00101

Notes

The authors declare no competing financial interest.

■ REFERENCES

(1) Gin, D. L.; Bara, J. E.; Noble, R. D.; Elliott, B. J. Polymerized lyotropic liquid crystal assemblies for membrane applications. *Macromol. Rapid Commun.* **2008**, *29*, 367−389.

(2) Li, L.; Schulte, L.; Clausen, L. D.; Hansen, K. M.; Jonsson, G. E.; Ndoni, S. Gyroid nanoporous membranes with tunable permeabilty. *ACS Nano* **2011**, *5*, 7754−7766.

(3) Ichikawa, T.; Kato, T.; Ohno, H. 3D continuous water nanosheet as a gyroid minimal surface formed by bicontinuous cubic liquid-crystalline zwitterions. *J. Am. Chem. Soc.* **2012**, *134*, 11354−11357.

(4) Jackson, G. L.; Perroni, D. V.; Mahanthappa, M. K. Roles of chemical functionality and pore curvature in the design of nanoporous proton conductors. *J. Phys. Chem. B* **2017**, *121*, 9429−9436.

(5) Jo, G.; Ahn, H.; Park, M. J. Simple route for tuning the morphology and conductivity of polymer electrolytes: one end functional group is enough. *ACS Macro Lett.* **2013**, *2*, 990−995.

(6) Kim, H.; Leal, C. Cuboplexes: topologically active siRNA delivery. *ACS Nano* **2015**, *9*, 10214−10226.

(7) Barriga, H. M. G.; Holme, M. N.; Stevens, M. M. Cubosomes: The next generation of smart lipid nanoparticles? *Angew. Chem., Int. Ed.* **2019**, *58*, 2958−2978.

(8) Hsueh, H.-Y.; Yao, C.-T.; Ho, R.-M. Well-ordered nanohybrids and nanoporous materials from gyroid block copolymer templates. *Chem. Soc. Rev.* **2015**, *44*, 1974−2018.

(9) Crossland, E. J. W.; Kamperman, M.; Nedelcu, M.; Ducati, C.; Wiesner, U.; Smilgies, G. E. S.; D-M; Toombes; Hillmyer, M. A.; Ludwigs, S.; Steiner, U.; Snaith, H. J. A bicontinuous double gyroid hybrid solar cell. *ACS Nano* **2009**, *9*, 2807−2812.

(10) Urbas, A. M.; Maldovan, M.; DeRege, P.; Thomas, E. L. Bicontinuous cubic block copolymer photonic crystals. *Adv. Mater.* **2002**, *14*, 1850−1853.

(11) Stefik, M.; Guldin, S.; Vignolini, S.; Wiesner, U.; Steiner, U. Block copolymer self-assembly for nanophotonics. *Chem. Soc. Rev.* **2015**, *44*, 5076−5091.

(12) Matsen, M. W.; Bates, F. S. Origins of complex self-assembly in block copolymers. *Macromolecules* **1996**, *29*, 7641−7644.

(13) Epps, T. H.; Cochran, E. W.; Bailey, T. S.; Waletzko, R. S.; Hardy, C. M.; Bates, F. S. Ordered network phases in linear poly(isoprene-*b*-styrene-*b*-ethylene oxide) triblock copolymers. *Macromolecules* **2004**, *37*, 8325−8341.

(14) Park, S. J.; Cheong, G. K.; Bates, F. S.; Dorfman, K. D. Stability of the double gyroid phase in bottlebrush diblock copolymer melts. *Macromolecules* **2021**, *54*, 9063−9070.

(15) Kawamoto, K.; Zhong, M.; Gadelrab, K. R.; Cheng, L.-C.; Ross, C. A.; Alexander-Katz, A.; Johnson, J. A. Graft-through synthesis and assembly of janus bottlebrush polymers from A-branch-B diblock macromonomers. *J. Am. Chem. Soc.* **2016**, *138*, 11501−11504.

(16) Rokhlenko, Y.; Kawamoto, K.; Johnson, J. A.; Osuji, C. O. Sub-10 nm self-assembly of mesogen-containing grafted macromonomers and their bottlebrush polymers. *Macromolecules* **2018**, *51*, 3680−3690.

(17) Jiang, L.; Nykypanchuk, D.; Pastore, V. J.; Rzayev, J. Morphological behavior of compositionally gradient polystyrene−polylactide bottlebrush copolymers. *Macromolecules* **2019**, *52*, 8217−8226.

(18) Chremos, A.; Theodorakis, P. E. Morphologies of bottle-brush block copolymers. *ACS Macro Lett.* **2014**, *3*, 1096−1100.

(19) Hashim, R.; Sugimura, A.; Minamikawa, H.; Heidelberg, T. Nature-like synthetic alkyl branched-chain glycolipids: A review on chemical structure and self-assembly properties. *Liq. Cryst.* **2012**, *39*, 1−17.

(20) Salim, M.; Wan Iskandar, W. F. N.; Patrick, M.; Zahid, N. I.; Hashim, R. Swelling of bicontinuous cubic phases in Guerbet glycolipid: Effects of additives. *Langmuir* **2016**, *32*, 5552−5561.

(21) Wan Iskandar, W. F. N.; Salim, M.; Hashim, R.; Zahid, N. I. Stability of cubic phase and curvature tuning in the lyotropic system of branched chain galactose-based glycolipid by amphiphilic additives. *Colloid Surf. A-Physicochem. Eng. Asp* **2021**, *623*, 126697.

(22) Duesing, P. M.; Templer, R. H.; Seddon, J. M. Quantifying Packing Frustration Energy in Inverse Lyotropic Mesophases. *Langmuir* **1997**, *13*, 351−359.

(23) Padmanabhan, P.; Chavis, M.; Ober, C. K.; Escobedo, F. A. Phase behaviour of PMMA-bPHEMA with solvents methanol and THF: Modelling and comparison to the experiment. *Soft Matter* **2014**, *10*, 6172−6181.

(24) Sinturel, C.; Bates, F. S.; Hillmyer, M. A. High χ-low *N* block polymers: How far can we go? *ACS Macro Lett.* **2015**, *4*, 1044−1050.

(25) Nunes, S. P. Block copolymer membranes for aqueous solution applications. *Macromolecules* **2016**, *49*, 2905−2916.

(26) Nickmans, K.; Schenning, A. P. H. J. Directed self-assembly of liquid-crystalline molecular building blocks for sub-5 nm nano-patterning. *Adv. Mater.* **2018**, *30*, 1703713.

(27) Jennings, J.; Green, B.; Mann, T. J.; Guymon, C. A.; Mahanthappa, M. K. Nanoporous polymer networks templated by gemini surfactant lyotropic liquid crystals. *Chem. Mater.* **2018**, *30*, 185−196.

(28) Durand, W. J.; Blachut, G.; Maher, M. J.; Sirard, S.; Tein, M. C.; Carlson, S.; Asano, Y.; Zhou, S. X.; Lane, A. P.; Bates, C. M.; Ellison, C. J.; Willson, C. G. Design of high-χ block copolymers for lithography. *J. Polym. Sci., Part A: Polym. Chem.* **2015**, *53*, 344−352.

(29) Cushen, J. D.; Otsuka, I.; Bates, C. M.; Halila, S.; Fort, S.; Rochas, C.; Easley, J. A.; Rausch, E. L.; Thio, A.; Borsali, R.; Willson, C. G.; Ellison, C. J. Oligosaccharide/silicon-containing block copolymers with 5 nm features for lithographic applications. *ACS Nano* **2012**, *6*, 3424−3433.

(30) Zha, R. H.; De Waal, B. F. M.; Lutz, M.; Teunissen, A. J. P.; Meijer, E. W. End groups of functionalized siloxane oligomers direct block-copolymeric or liquid-crystalline self-assembly Behavior. *J. Am. Chem. Soc.* **2016**, *138*, 5693−5698.

(31) Legrain, A.; Fleury, G.; Mumtaz, M.; Navarro, C.; Arias-Zapata, J.; Chevalier, X.; Cayrefourcq, I.; Zelsmann, M. Straightforward integration flow of a silicon-containing block copolymer for line space patterning. *ACS Appl. Mater. Interfaces* **2017**, *9*, 43043−43050.

(32) van Genabeek, B.; de Waal, B. F. M.; Gosens, M. M. J.; Pitet, L. M.; Palmans, A. R. A.; Meijer, E. W. Synthesis and self-assembly of discrete dimethylsiloxane−lactic acid diblock co-oligomers: The

dononacontamer and its shorter homologues. *J. Am. Chem. Soc.* **2016**, *138*, 4210−4218.

(33) Oschmann, B.; Lawrence, J.; Schulze, M. W.; Ren, J. M.; Anastasaki, A.; Luo, Y.; Nothling, M. D.; Pester, C. W.; Delaney, K. T.; Connal, L. A.; McGrath, A. J.; Clark, P. G.; Bates, C. M.; Hawker, C. J. Effects of tailored dispersity on the self-assembly of dimethylsiloxane-methyl methacrylate block co-oligomers. *ACS Macro Lett.* **2017**, *6*, 668−673.

(34) Ren, Y.; Lodge, T. P.; Hillmyer, M. A. A simple and mild route to highly fluorinated model polymers. *Macromolecules* **2001**, *34*, 4780−4787.

(35) Kennemur, J. G.; Yao, L.; Bates, F. S.; Hillmyer, M. A. Sub-5 nm domains in ordered poly(cyclohexylethylene)-block-poly(methyl methacrylate) block polymers for lithography. *Macromolecules* **2014**, *47*, 1411−1418.

(36) Otsuka, I.; Zhang, Y.; Isono, T.; Rochas, C.; Kakuchi, T.; Satoh, T.; Borsali, R. Sub-10 nm scale nanostructures in self-organized linear di- and triblock copolymers and miktoarm star copolymers consisting of maltoheptaose and polystyrene. *Macromolecules* **2015**, *48*, 1509−1517.

(37) Schmitt, A. K.; Mahanthappa, M. K. Order and disorder in high χ/low N, broad dispersity ABA triblock polymers. *Macromolecules* **2017**, *50*, 6779−6787.

(38) Nowak, S. R.; Lachmayr, K. K.; Yager, K. G.; Sita, L. R. Stable thermotropic 3D and 2D double gyroid nanostructures with sub-2-nm feature size from scalable sugar−polyolefin conjugates. *Angew. Chem., Int. Ed.* **2021**, *60*, 8710−8716.

(39) Chen, C.; Kieffer, R.; Ebert, H.; Prehm, M.; Zhang, R.-b.; Zeng, X.; Liu, F.; Ungar, G.; Tschierske, C. Chirality induction through nano-phase separation: alternating network gyroid phase by thermotropic self-sssembly of X-shaped bolapolyphiles. *Angew. Chem., Int. Ed.* **2020**, *59*, 2725−2729.

(40) Zeng, X.; Prehm, M.; Ungar, G.; Tschierske, C.; Liu, F. Formation of a double diamond cubic phase by thermotropic liquid crystalline self-assembly of bundled bolaamphiphiles. *Angew. Chem., Int. Ed.* **2016**, *55*, 8324−8327.

(41) Zeng, X.; Poppe, S.; Lehmann, A.; Prehm, M.; Chen, C.; Liu, F.; Lu, H.; Ungar, G.; Tschierske, C. A self-assembled bicontinuous cubic phase with a single-diamond network. *Angew. Chem., Int. Ed.* **2019**, *58*, 7375−7379.

(42) Liu, F.; Prehm, M.; Zeng, X.; Tschierske, C.; Ungar, G. Skeletal cubic, lamellar, and ribbon phases of bundled thermotropic bolapolyphiles. *J. Am. Chem. Soc.* **2014**, *136*, 6846−6849.

(43) Chen, Q. P.; Barreda, L.; Oquendo, L. E.; Hillmyer, M. A.; Lodge, T. P.; Siepmann, J. I. Computational design of high-χ block oligomers for accessing 1 nm domains. *ACS Nano* **2018**, *12*, 4351−4361.

(44) Barreda, L.; Shen, Z.; Chen, Q. P.; Lodge, T. P.; Siepmann, J. I.; Hillmyer, M. A. Synthesis, simulation, and self-assembly of a model amphiphile to push the limits of block polymer nanopatterning. *Nano Lett.* **2019**, *19*, 4458−4462.

(45) Shen, Z.; Chen, J. L.; Vernadskaia, V.; Ertem, S. P.; Mahanthappa, M. K.; Hillmyer, M. A.; Reineke, T. M.; Lodge, T. P.; Siepmann, J. I. From order to disorder: computational design of triblock amphiphiles with 1 nm domains. *J. Am. Chem. Soc.* **2020**, *142*, 9352−9362.

(46) Hentrich, F.; Diele, S.; Tschierske, C. Thermotropic liquid crystalline properties of 1,2,ψ, ω-*n*-alkan-tetraols. *Liq. Cryst.* **1994**, *17*, 827−839.

(47) Tanaka, H.; Hasegawa, H.; Hashimoto, T. Ordered structure in mixtures of a block copolymer and homopolymers. 1. Solubilization of low-molecular-weight homopolymers. *Macromolecules* **1991**, *24*, 240−251.

(48) Hashimoto, T.; Yamasaki, K.; Koizumi, S.; Hasegawa, H. Ordered structure in blends of block copolymers. 1. Miscibility criterion for lamellar block copolymers. *Macromolecules* **1993**, *26*, 2895−2904.

(49) Hashimoto, T.; Koizumi, S.; Hasegawa, H. Ordered structure in blends of block copolymers. 2. Self-assembly for immiscible lamella-forming copolymers. *Macromolecules* **1994**, *27*, 1562−1570.

(50) Yamaguchi, D.; Bodycomb, J.; Koizumi, S.; Hashimoto, T. Ordered structure in blends of block copolymers. 4. Location of the short diblock. *Macromolecules* **1999**, *32*, 5884−5894.

(51) Ahn, S.; Kwak, J.; Choi, C.; Seo, Y.; Kim, J. K.; Lee, B. Gyroid structures at highly asymmetric volume fractions by blending of ABC triblock terpolymer and AB diblock copolymer. *Macromolecules* **2017**, *50*, 9008−9014.

(52) Choi, C.; Ahn, S.; Kim, J. K. Diverse morphologies of block copolymers by blending with homo (and co) polymers. *Macromolecules* **2020**, *53*, 4577−4580.

(53) Ahn, J.-H.; Zin, W.-C. Structure of shear-induced perforated layer phase in styrene−isoprene diblock copolymer melts. *Macromolecules* **2000**, *33*, 641−644.

(54) Shen, Z.; Sun, Y.; Lodge, T. P.; Siepmann, J. I. Development of a PointNet for Detecting Morphologies of Self- Assembled Block Oligomers in Atomistic Simulations. *J. Phys. Chem. B* **2021**, *125*, 5275−5284.

(55) Matsen, M. W.; Bates, F. S. Block copolymer microstructures in the intermediate-segregation regime. *J. Chem. Phys.* **1997**, *106*, 2436−2448.

(56) Lai, C. T.; Shi, A.-C. Binary blends of diblock copolymers: An effective route to novel bicontinuous phases. *Macromol. Theory Simul.* **2021**, *30*, 2100019.

(57) Khandpur, A. K.; Foerster, S.; Bates, F. S.; Hamley, I. W.; Ryan, A. J.; Bras, W.; Almdal, K.; Mortensen, K. Polyisoprene-Polystyrene Diblock Copolymer Phase Diagram near the Order-Disorder Transition. *Macromolecules* **1995**, *28*, 8796−8806.

(58) Matsen, M. W. Stabilizing new morphologies by blending homopolymer with block copolymer. *Phys. Rev. Lett.* **1995**, *74*, 4225−4228.

(59) Matsen, M. W. Effect of architecture on the phase behavior of AB-type block copolymer melts. *Macromolecules* **2012**, *45*, 2161−2165.

(60) Matsen, M. W.; Bates, F. S. Conformationally asymmetric block copolymers. *J. Polym. Sci. B Polym. Phys.* **1997**, *35*, 945−952.

(61) Milner, S. T. Chain architecture and asymmetry in copolymer microphases. *Macromolecules* **1994**, *27*, 2333−2335.

(62) Xie, N.; Li, W.; Qiu, F.; Shi, A.-C. σ phase formed in conformationally asymmetric AB-type block copolymers. *ACS Macro Lett.* **2014**, *3*, 906−910.

(63) Van Der Spoel, D.; Lindahl, E.; Hess, B.; Groenhof, G.; Mark, A. E.; Berendsen, H. J. C. GROMACS: Fast, flexible, and free. *J. Comput. Chem.* **2005**, *26*, 1701−1718.

(64) Abraham, M. J.; Murtola, T.; Schulz, R.; Páll, S.; Smith, J. C.; Hess, B.; Lindahl, E. GROMACS: High performance molecular simulations through multi-level parallelism from laptops to super-computers. *SoftwareX* **2015**, *1−2*, 19−25.

(65) Nosé, S. A unified formulation of the constant temperature molecular dynamics methods. *J. Chem. Phys.* **1984**, *81*, 511−519.

(66) Hoover, W. G. Canonical dynamics: equilibrium phase-space distributions. *Phys. Rev. A* **1985**, *31*, 1695−1697.

(67) Parrinello, M.; Rahman, A. Polymorphic transitions in single crystals: A new molecular dynamics method. *J. Appl. Phys.* **1981**, *52*, 7182−7190.

(68) Essmann, U.; Perera, L.; Berkowitz, M. L.; Darden, T.; Lee, H.; Pedersen, L. G. A smooth particle mesh Ewald method. *J. Chem. Phys.* **1995**, *103*, 8577−8593.

(69) Hess, B. P−LINCS: A parallel linear constraint solver for molecular simulation. *J. Chem. Theory Comput.* **2008**, *4*, 116−122.

(70) Martin, M.; Siepmann, J. Novel configurational-bias monte carlo method for branched Molecules. Transferable potentials for phase equilibria. 2. United-Atom description of branched alkanes. *J. Phys. Chem. B* **1999**, *103*, 4508−4517.

(71) Stukowski, A. Visualization and analysis of atomistic simulation data with OVITO-the Open Visualization Tool. *Model. Simul. Mater. Sci. Eng.* **2010**, *18*, 015012.

(72) Humphrey, W.; Dalke, A.; Schulten, K. VMD − Visual Molecular Dynamics. *J. Mol. Graphics* **1996**, *14*, 33−38.

(73) Arora, A.; Morse, D. C.; Bates, F. S.; Dorfman, K. D. Commensurability and finite size effects in lattice simulations of diblock copolymers. *Soft Matter* **2015**, *11*, 4862−4867.

(74) Glaser, J.; Qin, J.; Medapuram, P.; Morse, D. C. Collective and single-chain correlations in disordered melts of symmetric diblock copolymers: quantitative comparison of simulations and theory. *Macromolecules* **2014**, *47*, 851−869.

(75) Dotera, T. Tricontinuous cubic structures in *ABC/A/C* copolymer and homopolymer blends. *Phys. Rev. Lett.* **2002**, *89*, 205502.

(76) Martínez-Veracoechea, F. J.; Escobedo, F. A. Simulation of the gyroid phase in off-lattice models of pure diblock copolymer melts. *J. Chem. Phys.* **2006**, *125*, 104907.

(77) Schönhöfer, P. W. A.; Ellison, L. J.; Marechal, M.; Cleaver, D. J.; Schröder-Turk, G. E. Purely entropic self-assembly of the bicontinuous Ia3̄d gyroid phase in equilibrium hard-pear systems. *Interface Focus* **2017**, *7*, 20160161.

(78) Hajduk, D. A.; Harper, P. E.; Gruner, S. M.; Honeker, C. C.; Kim, G.; Thomas, E. L.; Fetters, L. J. The gyroid: A new equilibrium morphology in weakly segregated diblock copolymers. *Macromolecules* **1994**, *27*, 4063−4075.

(79) Luo, K.; Shen, Z.; Das, S.; Jaye, J.; Li, D.; Reineke, T. M.; Calabrese, M.; Mahanthappa, M. K.; Siepmann, J. I. A Computational Workflow for Exploring the Self-assembly of Glycolipids into Three-dimensional Network Phases. In preparation.

(80) Brigham, E. O.; Morrow, R. E. The fast Fourier transform. *IEEE Spectrum* **1967**, *4*, 63−70.

(81) Qi, C. R.; Su, H.; Mo, K.; Guibas, L. J. PointNet: Deep Learning on Point Sets for 3D Classification and Segmentation. *arXiv*, 2016, 1612.00593.

(82) DeFever, R. S.; Targonski, C.; Hall, S. W.; Smith, M. C.; Sarupria, S. A generalized deep learning approach for local structure identification in molecular simulations. *Chem. Sci.* **2019**, *10*, 7503−7515.

(83) Kingma, D. P.; Ba, J. Adam: A method for stochastic optimization. *arXiv*, 1412.6980, 2014.

(84) Cheong, G. K.; Chawla, A.; Morse, D. C.; Dorfman, K. D. Open-source code for self-consistent field theory calculations of block polymer phase behavior on graphics processing units. *Eur. Phys. J. E* **2020**, *43*, 15.

(85) Arora, A.; Qin, J.; Morse, D. C.; Delaney, K. T.; Fredrickson, G. H.; Bates, F. S.; Dorfman, K. D. Broadly accessible self-consistent field theory for block polymer materials discovery. *Macromolecules* **2016**, *49*, 4675−4690.

(86) Ranjan, A.; Qin, J.; Morse, D. C. Linear response and stability of ordered phases of block copolymer melts. *Macromolecules* **2008**, *41*, 942−954.

(87) Arora, A.; Morse, D. C.; Bates, F. S.; Dorfman, K. D. Accelerating self-consistent field theory of block polymers in a variable unit cell. *J. Chem. Phys.* **2017**, *146*, 244902.